Copyright © 2024 IEEE. DOI 10.1109/JCS61227.2024.10646192. Personal use of this material is permitted. Permission from IEEE must be obtained for all other uses, in any current or future media, including reprinting/republishing this material for advertising or promotional purposes, creating new collective works, for resale or redistribution to servers or lists, or reuse of any copyrighted component of this work in other works.

Circularly Polarized Dual Antenna with Crescent Axed Sporadic Meander Traces Isolated by Shorting Pins and Defected Ground for Wi-Fi Sensing

Shahanawaz Kamal, Jan Adler, Maximilian Matthé, and Padmanava Sen

Barkhausen Institut, 01067 Dresden, Germany
Emails: {shahanawaz.kamal, jan.adler, maximilian.matthe, padmanava.sen}@barkhauseninstitut.org

***Abstract*—This paper introduces a dual-element multiple-input−multiple-output (MIMO) microstrip antenna for device-to-device (D2D) integrated sensing and communications (ISAC) applications in the Wi-Fi 6 GHz spectrum. Each radiating element was equipped with a feeding port on one of its ends that was connected to a quarter-wavelength (0.25λ) line for impedance matching. The 0.25λ line was subsequently coupled to a crescent axed sporadic meander trace for attaining circular polarization (CP) and antenna miniaturization. In particular, axial ratio (AR) of <3 dB was realized in a compact area of 5.3 cm × 5.3 cm that is 1.1λ × 1.1λ at the center frequency (f_{center}) of 6.33 GHz. A rectangular microstrip was integrated between the two radiating elements, and at the same time, along the edge of the dielectric substrate to render a parasitic resonance that ultimately contributed in producing the omnidirectional circularly polarized (OCP) electromagnetic (EM) waves. Furthermore, a decoupling architecture composed of multiple shorting pins that extended from the parasitic element to the defected ground was introduced for accomplishing a high average isolation of >20 dB. Flame-resistant (FR-4), an inexpensive dielectric substrate with low-profile of 0.03λ was used to yield a wide impedance bandwidth (I-BW) ranging from 4.42 GHz − 8.24 GHz. The simulated computations, and the measurement results procured within the anechoic chamber confirmed substantial agreement. Moreover, lab experiments proved the suitability of the manufactured antenna for communications applications. In contrast with contemporary antennas, the proposed antenna occupied small area and low-profile to exhibit a wide axial ratio bandwidth (AR-BW) that combines with reasonable performance in terms of I-BW and average isolation.**

***Index Terms*—Antenna, circular polarization, isolation, integrated sensing and communications, low-profile, miniature, multiple-input−multiple-output, omnidirectional, wideband.**

I. Introduction

Recently, worldwide technological research has been focused to embrace the period of ISAC using the EM waves for monitoring health conditions, navigation, positioning, and activity recognition among many other facets of daily life [1]. The deployment of ISAC features ought to be enabled by utilizing the existing EM spectrum, control framework, signal processing method, and hardware platform. Wi-Fi signals stand out amongst other ISAC mediums for their widespread presence, durability against environmental factors, and inexpensive hardware cost. Specifically, Wi-Fi enabled gadgets are projected to share the 6 GHz EM spectrum with licensed and license-exempt incumbents [2]. However, license-exempt appliances typically adhere to indoor operations with limitations on peak radiated power to safeguard the existing services. Furthermore, Wi-Fi signals unavoidably face numerous obstacles while being sent or detected, which results in the multipath effect and ultimately causes the monitoring system to malfunction [3].

978-8-3503-8544-1/24/$31.00 ©2024 IEEE

Wi-Fi-based ISAC solutions in a spectrum-sharing environment rely substantially on the performance of antennas [4], [5]. Particularly, antennas exhibiting the following features are vital for D2D ISAC scenario. (a) Microstrip-based architecture to reduce the antenna footprint while facilitating seamless integration alongside other circuits [6]. (b) MIMO antennas to improve the quality, capacity, and reliability of the EM communications [7]. (c) High isolation to mitigate the mutual coupling caused when MIMO antenna elements are packed closely together in a small region [8]. (d) OCP radiation pattern to prevent multipath interference and ensure stable network connectivity in all directions [9], [10]. (e) Wide I-BW to investigate every potential open channel possibility when conducting an exploratory scan for spectrum-sharing [11].

A conventional MIMO antenna doesn't isolate OCP EM waves adequately and independently [12], [13]. Typically, the antenna design and/or material undergoes modifications to improve the envisioned performance metrics. A range of microstrip-based MIMO antennas that address the aforementioned challenges are covered in the literature. One technique in a bid to improve isolation in a four-port MIMO antenna operating from 2.45 GHz − 7.45 GHz entails altering the ground plane [14]. However, this antenna is not ideal for Wi-Fi sensing due to its linearly polarized radiation pattern and limited average isolation of 12 dB. While adopting an identical methodology, a two-port MIMO antenna yielded OCP EM waves with relatively high average isolation of 20 dB [15]. But, the accomplishment endured narrow AR-BW that is from 2.7 GHz − 4.38 GHz only. The EM bandgap approach demonstrates an effective method for realizing average isolation of 40 dB in an eight-port CP MIMO antenna [16]. Nevertheless, the antenna geometry needs a large area of 2λ × 2λ to operate exclusively from 6.0 GHz − 6.4 GHz. In contrast, a minor

Copyright © 2024 IEEE. DOI 10.1109/JCS61227.2024.10646192. Personal use of this material is permitted. Permission from IEEE must be obtained for all other uses, in any current or future media, including reprinting/republishing this material for advertising or promotional purposes, creating new collective works, for resale or redistribution to servers or lists, or reuse of any copyrighted component of this work in other works.

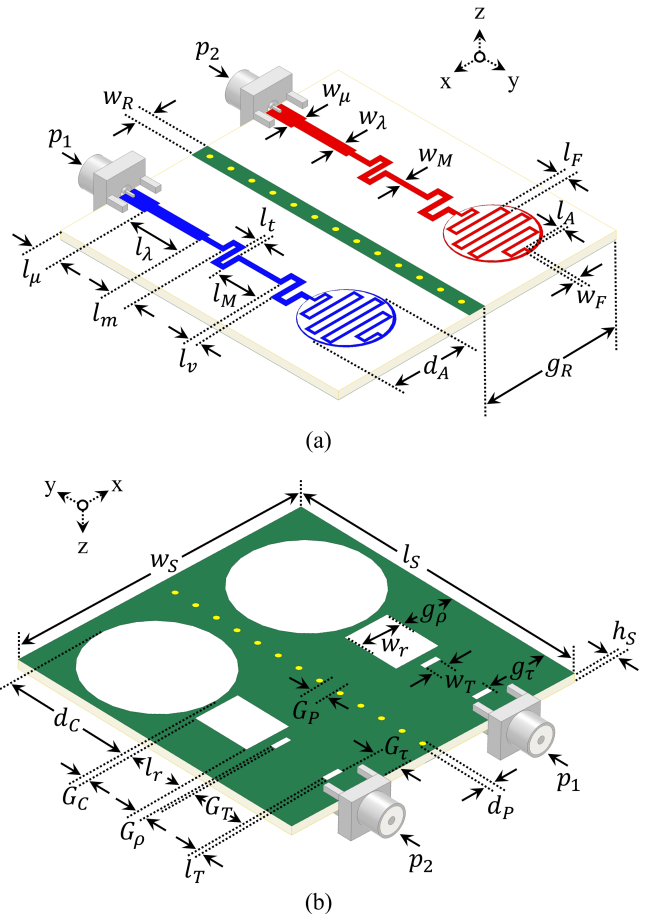

Fig. 1. (a) Top and (b) bottom configuration of the proposed antenna.

reduction in the antenna size of $1.9\lambda \times 1.9\lambda$ with I-BW from 5.6 GHz − 6.1 GHz became apparent when a dual-port MIMO setup was created by stacking dielectric layers of the ground plane, feed network, EM bandgap surface, and air cavity [17]. On the other hand, 40 dB of average isolation was ascertained for merely 240 MHz, and both their overall profile and level of design complexity increased. Another dual-port MIMO antenna that integrated defected ground and shorting pins to realize OCP EM waves from 4.24 GHz − 5.38 GHz in a compact layout of $0.5\lambda \times 0.4\lambda$ could only achieve an average isolation of 15 dB [18].

This paper presents a novel microstrip-based dual-port MIMO antenna design for ISAC in the Wi-Fi 6 GHz spectrum. The proposed antenna exhibits compact size of $1.1\lambda \times 1.1\lambda$, low-profile of 0.03λ, wide I-BW from 4.42 GHz − 8.24 GHz, high average isolation of >20 dB, and OCP radiation pattern. The strategic integration of different segments like the 0.25λ line, crescent axed sporadic meander trace, parasitic element, and decoupling network into the antenna design resulted in the realization of all of these features. Additionally, with minimal fabrication losses, the proposed design is straightforward and inexpensive to build.

TABLE I
PROPOSED ANTENNA PARAMETER VALUES IN λ AT 6.33 GHZ

l_S 1.11	w_S 1.11	l_μ 0.10	w_μ 0.06	l_λ 0.25	w_λ 0.04	l_m 0.08	l_M 0.14	w_M 0.02	l_t 0.01
l_v 0.04	l_F 0.04	w_F 0.01	l_A 0.01	d_A 0.28	w_R 0.06	g_R 0.52	d_p 0.02	G_p 0.08	l_T 0.02
w_T 0.06	G_τ 0.09	g_τ 0.25	G_T 0.18	l_r 0.21	w_r 0.16	G_ρ 0.03	g_ρ 0.18	d_C 0.46	g_C 0.02

II. ANTENNA CONFIGURATION AND DESIGN

The configuration of the proposed microstrip-based antenna is demonstrated in Fig. 1 and their corresponding parameter values are listed in Table I. The antenna incorporated a dielectric substrate that featured a low-profile and small area. A printed circuit board made of FR-4 material having substrate height (h_S) of 0.03λ, dielectric constant (ϵ_r) of 4.4 and loss tangent (tan δ) of 0.02 was used in light of its superior I-BW behavior and low production cost.

The dimensions of the antenna may be approximated through the concepts of microstrip transmission line [19], interdigital capacitor [20], meander line [21], defected ground [22], and mushroom-shaped EM bandgap [23].

The characteristic impedance (Z_0) of microstrip transmission lines may be estimated through the next equations [19].

$$Z_0 = \frac{60}{\sqrt{\epsilon_{re}}} \ln \frac{5.98 \times h_S}{(0.8 \times w_S) + (w_{\mu,\lambda,M,F})} \tag{1}$$

$$\epsilon_{re} = (0.475 \times \epsilon_r) + 0.67 \tag{2}$$

where, ϵ_{re} indicates the effective dielectric constant relative to air.

Typically, the conducting elements and inter-element spacing are respectively described by inductance (L) and capacitance (C) using the approximations stated below [21].

$$L \approx \frac{\mu_0 \times (w_M + l_t, w_M + l_v, l_F)}{2 \times \pi} \ln \frac{2 \times (w_M + l_t, w_M + l_v, l_F)}{\pi \times (w_{\mu,\lambda,M,F})} \tag{3}$$

$$C \approx 4 \frac{\epsilon_0 \times (w_M + l_t, w_M + l_v, l_F)}{2 \times \pi} \ln \frac{2 \times (w_M + l_t, w_M + l_v, l_F)}{\pi \times (l_{t,v,A})} \tag{4}$$

where, μ_0 and ϵ_0 expresses the permeability and permittivity of the vacuum, respectively.

A. Radiation Surface

The radiation surface was made up of two identical microstrip elements that were positioned side by side to accomplish the benefits of the MIMO technology. Each of the radiating elements was fed from the same end of the dielectric substrate that was attached to a 0.25λ line. An appropriate impedance matching was yielded by integrating a 0.25λ line that connected the remaining portion of the radiating element.

The electrical dimensions of the antenna was increased while keeping their physical extents short by integrating meandering traces crafted by twisting conductors. Additionally, the

Copyright © 2024 IEEE. DOI 10.1109/JCS61227.2024.10646192. Personal use of this material is permitted. Permission from IEEE must be obtained for all other uses, in any current or future media, including reprinting/republishing this material for advertising or promotional purposes, creating new collective works, for resale or redistribution to servers or lists, or reuse of any copyrighted component of this work in other works.

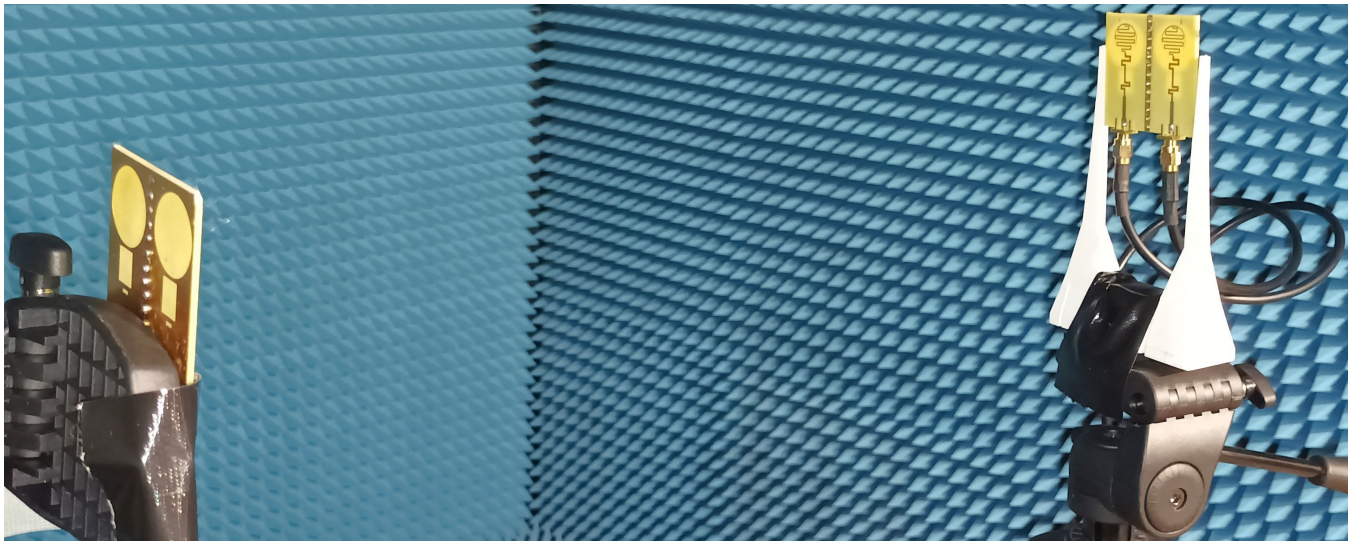

Fig. 2. Photograph of the proposed antenna under measurement.

radiation surface was meticulously designed to produce CP EM waves. Descriptively, the meandering microstrip exhibit a non-uniform pattern that split into four sections. The first portion dealt with creating a change in the direction of current flow by twisting the conductor in the opposite direction. The second part focused on the trace size, and it involved the implementation of a fat conductor followed by a thin track. The third section addressed the geometry of meander line, specifically the narrowest microstrip was designed with a circular pattern. The final region represented a crescent-shaped line that ended the circuit at the third segment.

A parasitic component composed of a rectangular track was integrated between the two radiating elements and across the length of the dielectric substrate. This configuration was considered to generate a parasitic resonance that eventually contributed in establishing OCP radiation pattern.

B. Decoupling Architecture

A decoupling architecture was built with two key components, namely shorting pins and a defected ground plane to reduce the mutual coupling of surface currents among the MIMO antenna elements. The number and placement of the shorting pins and slots were decided strategically to achieve high average isolation without interfering with the primary resonance. A series of shorting pins were incorporated that extended from the parasitic element to the defected ground plane. This configuration contributed to increase the polarization angle, making the two radiating elements orthogonal to their counterparts and enabling good antenna diversity. Slots were added to the ground plane at four key positions below each radiating element to create defects that ultimately avoid the propagation of the surface currents amid the two radiating parts. In particular, the 0.25λ (at 6.33 GHz) line's two transition regions were covered by two small rectangular slots. Furthermore, the area right above the the 0.25λ line was encompassed by a rectangular slot. Finally, the latter two

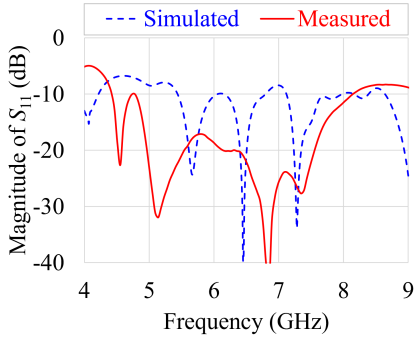

Fig. 3. Simulated and measured $|S_{11}|$ of the proposed antenna.

sections, which were made up of the narrowest meander line and the crescent axed microstrip, were entirely concealed by a circular slot.

III. Antenna Results and Discussion

The antenna simulations were carried out with the aid of Ansys high-frequency structure simulator (HFSS). The proposed antenna was fabricated by leveraging the standard photolithography technique. Their measurements were taken in the anechoic chamber at Barkhausen Institut, Germany to validate the simulation results. A picture of the fabricated antenna under measurement is shown in Fig. 2. Overall, there was a good agreement between the simulation and measurement results; but, discrepancies in nature or range of results were detected because of flaws in the manufacturing process, termination resistance or connector tolerances, improper alignment and unwanted radiations from the feed cable.

Fig. 3 displays the $|S_{11}|$ as a function of frequency. The proposed antenna was properly matched in the Wi-Fi 6 GHz spectrum. A wide -10 dB I-BW was accomplished that extended from 4.42 GHz $-$ 8.24 GHz. The $|S_{21}|$ variation over frequency is shown in Fig. 4. A high average isolation of >20

Copyright © 2024 IEEE. DOI 10.1109/JCS61227.2024.10646192. Personal use of this material is permitted. Permission from IEEE must be obtained for all other uses, in any current or future media, including reprinting/republishing this material for advertising or promotional purposes, creating new collective works, for resale or redistribution to servers or lists, or reuse of any copyrighted component of this work in other works.

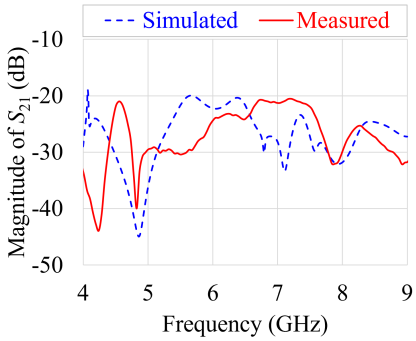

Fig. 4. Simulated and measured $|S_{21}|$ of the proposed antenna.

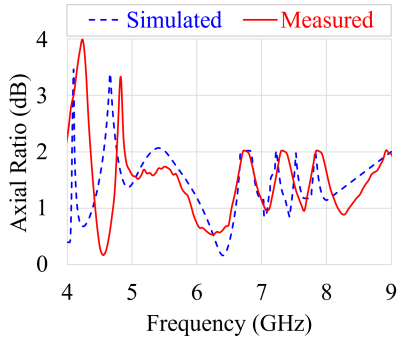

Fig. 5. Simulated and measured AR of the proposed antenna.

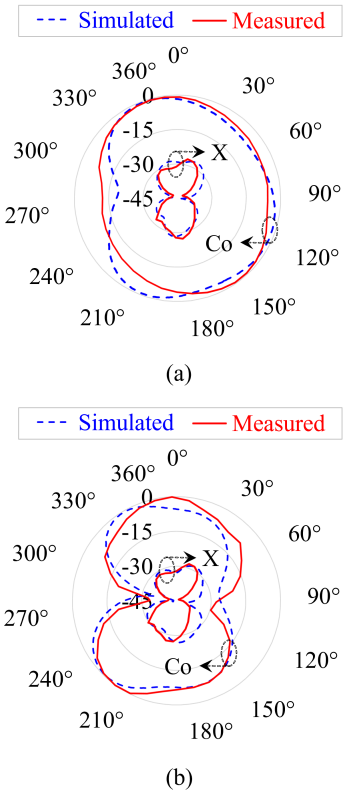

Fig. 6. Simulated and measured radiation patterns of the proposed antenna at 6.33 GHz in the (a) azimuth plane and (b) elevation plane.

dB was yielded. The AR changes against frequency are shown in Fig. 5. The AR measurements in the functional band were <3 dB, that confirmed the CP performance. Fig. 6(a) and Fig. 6(b) demonstrate the right (Co)/left (X) hand (LHCP) radiation patterns at 6.33 GHz, respectively, in the azimuth plane and elevation plane. Good OCP performance was ascertained. Fig. 7 and Fig. 8 prove that the proposed antenna accomplished reasonable gain and efficiency values of ≈4 dBi and ≈65% in the operating frequency band, respectively.

To further demonstrate the proposed antenna's communication performance, the Heterogeneous Radio Mobile Simulator Python [24] (Hermes) was configured to generate Orthogonal Frequency Division Multiplexing (OFDM) frames featuring 2048 subcarriers spaced 240 kHz apart, the center 1024 of which were populated so that the OFDM frames' overall effective bandwidth was 245.76 MHz. Each frame consisted of a pilot symbol for synchronization, followed by 30 16-QAM modulated data symbols prepended by a cyclic prefix of 140 samples, leading to a frame duration of ≈ 138 μs. Two units of the proposed antenna were placed ≈ 2 m apart and connected to the first four antenna ports of an Ettus X410 [25] Universal Software-Defined Radio Peripheral (USRP), as depicted in Fig. 2. While successively increasing the USRP's transmit power gain from 45 dB to 60 dB in 1 dB steps, 100 frames were exchanged between a pair of antennas, each antenna being located in a dedicated unit. The process was repeated for three carrier frequency candidates $f_{center} \in \{5.2\text{ GHz}, 6.2\text{ GHz}, 7.2\text{ GHz}\}$.

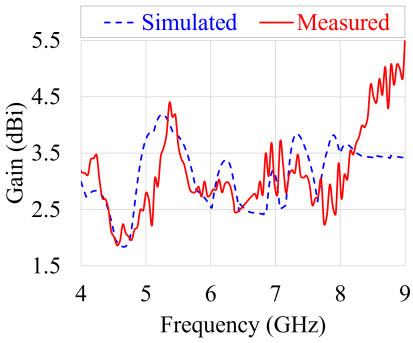

Fig. 7. Simulated and measured gain of the proposed antenna.

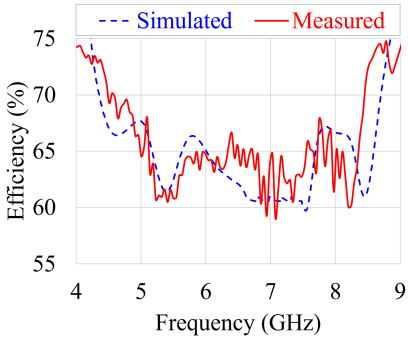

Fig. 8. Simulated and measured efficiency of the proposed antenna.

Copyright © 2024 IEEE. DOI 10.1109/JCS61227.2024.10646192. Personal use of this material is permitted. Permission from IEEE must be obtained for all other uses, in any current or future media, including reprinting/republishing this material for advertising or promotional purposes, creating new collective works, for resale or redistribution to servers or lists, or reuse of any copyrighted component of this work in other works.

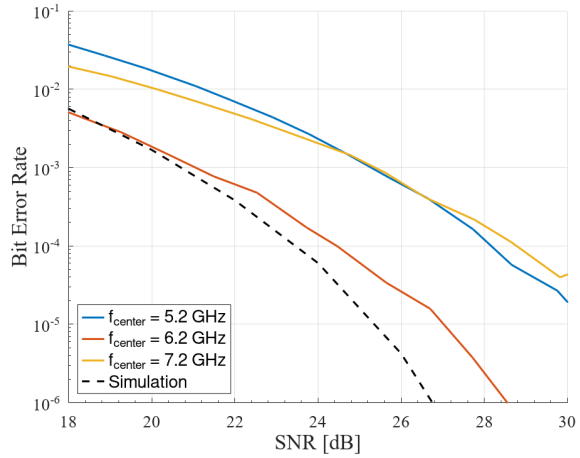

Fig. 9. Communication performance of the proposed antenna.

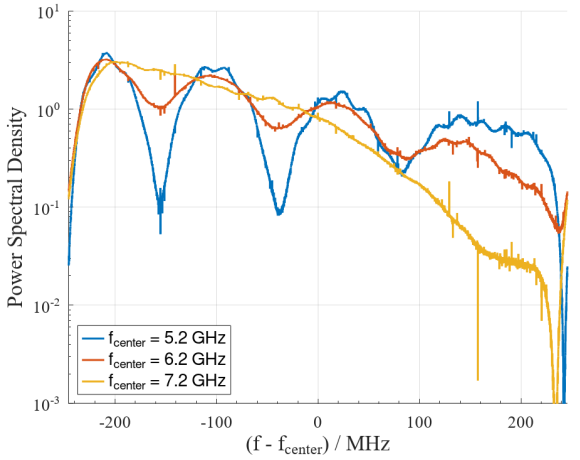

Fig. 10. Communication link frequency selectivity using the proposed antenna.

In order to properly compare the three selected carrier frequencies of interest, the expected noise powers were estimated beforehand by recording the receive analog-digital converter's output with no transmission and the received signal powers during frame exchange, so that an estimate of the signal-to-noise ratio (SNR) for each carrier frequency could be obtained. The measured bit error rates for each carrier frequency with respect to the estimated SNRs are visualized in Fig. 9 and compared to a simulation of a flat (in frequency domain) channel introducing only additive white Gaussian noise at the receiver side, obtained by running Hermes' simulation pipeline with an OFDM configuration identical to the measurement setup's configuration.

The frequency response of the measurement setup's antenna link was estimated by transmitting 100 frames consisting of 10^4 samples of white noise and dividing the received signal's Discrete Fourier Transform (DFT) by the transmitted signal's DFT, followed by taking the mean over all frames. The resulting power spectral density estimate, normalized to unit power, is visualized in Fig. 10.

At 6.2 GHz carrier frequency, the proposed antenna performed comparable to the simulation predictions. However, at 5.2 GHz and 7.2 GHz the communication performance degraded, which is due to the increased frequency-selectivity around these bands (see Fig. 10) because of environmental effects. There, severely attenuated subcarriers increase the bit error rates for a given average SNR.

TABLE II
PERFORMANCE COMPARISON

Reference	f_{center} (GHz)	I-BW (%)	AR-BW (%)	$\lvert S_{21}\rvert$ (dB)	Footprint (λ^2)	Profile (λ)
[14]	4.9	101	Linear ↓	12 ↓	0.6×0.6	0.03
[15]	3.58	146	47 ↓	20	0.1×0.1	0.02
[16]	6.2	6.4 ↓	6.4 ↓	40	2.0×2.0 ↑	0.03
[17]	5.8	8.5 ↓	0.04 ↓	40	1.9×1.9 ↑	0.11 ↑
[18]	4.81	23.7 ↓	Linear ↓	15 ↓	0.5×0.4	0.01
Proposed	6.33	60.63	60.63	20	1.1×1.1	0.03

↓ indicates a poor performance metric in contrast to the proposed antenna.
↑ signifies a large footprint or profile relative to the proposed antenna.

IV. BENCHMARKING

In order to demonstrate the significance of this work, the proposed antenna has been compared with recently published MIMO antennas in Table II. Comparative analysis has focused on performance measures including I-BW, AR-BW, average isolation ($|S_{21}|$), footprint, and profile. Furthermore, the center frequencies of antennas are listed in the table for a legitimate comparison. Correspondingly, footprints and profiles of antennas were computed at the center frequency. The proposed antenna represents competitive with regard to AR-BW and exhibits a reasonable performance in the other considered metrics. A poor performance metric and a large footprint/profile need of a referenced antenna has been highlighted in the table with a down (↓) arrow and an up (↑) arrow, respectively.

V. CONCLUSION

The goal of developing a MIMO antenna that exhibits high average isolation and OCP EM waves in the 6 GHz band has been achieved. The proposed antenna encompassed a micorstrip-based dual-port architecture for enabling the advantages of MIMO technology with easy circuit integration capability. Meandered radiating traces were strategically modeled to attain miniaturization and CP EM waves. A parasitic element was integrated between the two radiating elements to enable OCP radiation pattern. A decoupling network of shorting pins and muliple defects in the ground was incorporated to achieve high average isolation. Measurements over the Ettus X410 software defined radio and accompanying simulation studies have been conducted to evaluate and validate the antenna configuration, design consideration and communication performance. The importance of the proposed antenna is proven by comparison with recently published antennas defining similar objectives. This work represents a competitive design that can be implemented and used for D2D ISAC using Wi-Fi signals.

Copyright © 2024 IEEE. DOI 10.1109/JCS61227.2024.10646192. Personal use of this material is permitted. Permission from IEEE must be obtained for all other uses, in any current or future media, including reprinting/republishing this material for advertising or promotional purposes, creating new collective works, for resale or redistribution to servers or lists, or reuse of any copyrighted component of this work in other works.

ACKNOWLEDGMENT

The project on which this publication is based was funded by the German Federal Ministry of Education and for Education and Research under the funding code 16KISK122. The responsibility for the content of this publication lies with the author.

REFERENCES

[1] J.-L. Huang, Y.-S. Wang, Y.-P. Zou, K.-S. Wu, and L. M.-s. Ni, "Ubiquitous wifi and acoustic sensing: Principles, technologies, and applications," *Journal of Computer Science and Technology*, vol. 38, no. 1, pp. 25–63, 2023.

[2] F. Meneghello, C. Chen, C. Cordeiro, and F. Restuccia, "Toward integrated sensing and communications in ieee 802.11 bf wi-fi networks," *IEEE Communications Magazine*, vol. 61, no. 7, pp. 128–133, 2023.

[3] G. Zhang, D. Zhang, Y. He, J. Chen, F. Zhou, and Y. Chen, "Passive human localization with the aid of reconfigurable intelligent surface," in *2023 IEEE Wireless Communications and Networking Conference (WCNC)*, pp. 1–6, IEEE, 2023.

[4] A. Raza, R. Keshavarz, E. Dutkiewicz, and N. Shariati, "Compact multi-service antenna for sensing and communication using reconfigurable complementary spiral resonator," *IEEE Transactions on Instrumentation and Measurement*, 2023.

[5] S. Kamal, M. F. B. Ain, U. Ullah, A. S. Mohammed, R. Hussin, M. F. B. M. Omar, F. Najmi, Z. A. Ahmad, M. F. Ab Rahman, M. N. Mahmud, *et al.*, "A low-profile quasi-loop magneto-electric dipole antenna featuring a wide bandwidth and circular polarization for 5g mmwave device-to-device communication," *Journal of Electromagnetic Engineering and Science*, vol. 22, no. 4, pp. 459–471, 2022.

[6] I. V. Triviño and A. K. Skrivervik, "Small antennas with broad beamwidth integrated on a drone enclosed in a protective structure," in *2023 17th European Conference on Antennas and Propagation (EuCAP)*, pp. 1–5, IEEE, 2023.

[7] F. Gao, L. Xu, and S. Ma, "Integrated sensing and communications with joint beam-squint and beam-split for mmwave/thz massive mimo," *IEEE Transactions on Communications*, 2023.

[8] A. Madni and W. T. Khan, "Design of a compact 4-element gnss antenna array with high isolation using a defected ground structure (dgs) and a microwave absorber," *IEEE Open Journal of Antennas and Propagation*, 2023.

[9] J. D. Peng, Q. Da Liu, L. H. Ye, X.-X. Tian, J.-F. Li, D.-L. Wu, and X. Y. Zhang, "Low-profile ultra-wideband dual-polarized omnidirectional antenna for indoor base station," *IEEE Transactions on Antennas and Propagation*, 2023.

[10] S. Kamal, M. F. Ain, U. Ullah, and M. F. M. Omar, "Enabling mimo antenna miniaturization and wide circular polarization coverage by amalgamation of a dielectric strip between meandered traces and slotted ground," *IEEE Antennas and Wireless Propagation Letters*, vol. 21, no. 9, pp. 1901–1905, 2022.

[11] P. K. Goswami and G. Goswami, "Wideband sensing antenna for smart cognitive radio applications," in *2020 9th International Conference System Modeling and Advancement in Research Trends (SMART)*, pp. 349–354, IEEE, 2020.

[12] U. Banerjee, A. Karmakar, and A. Saha, "A review on circularly polarized antennas, trends and advances," *International Journal of Microwave and Wireless Technologies*, vol. 12, no. 9, pp. 922–943, 2020.

[13] M. T. Yalcinkaya, P. Sen, and G. Fettweis, "Comparative analysis of antenna isolation characteristic with & without self-interference reduction techniques towards in-band full-duplex operation," *IET Microwaves, Antennas & Propagation*, vol. 17, no. 5, pp. 329–342, 2023.

[14] S. K. Mahto, A. K. Singh, R. Sinha, M. Alibakhshikenari, S. Khan, and G. Pau, "High isolated four element mimo antenna for ism/lte/5g (sub-6ghz) applications," *IEEE Access*, 2023.

[15] M. Kaushik, J. K. Dhanoa, and M. K. Khandelwal, "Partially omnidirectional and circularly polarized mimo antenna covering sub-6 ghz band for 5g fast plan," *IEEE Transactions on Components, Packaging and Manufacturing Technology*, 2023.

[16] M. R. Nikkhah, J. Wu, H. Luyen, and N. Behdad, "A concurrently dual-polarized, simultaneous transmit and receive (star) antenna," *IEEE Transactions on Antennas and Propagation*, vol. 68, no. 8, pp. 5935–5944, 2020.

[17] L. Ma, J. Lu, C. Gu, and J. Mao, "A wideband dual-circularly polarized, simultaneous transmit and receive (star) antenna array for integrated sensing and communication in iot," *IEEE Internet of Things Journal*, vol. 10, no. 7, pp. 6367–6376, 2022.

[18] P. Jha, A. Kumar, and A. De, "Two-port miniaturized textile antenna for 5g and wlan applications," *International Journal of Microwave and Wireless Technologies*, pp. 1–10, 2023.

[19] H. Kaupp, "Characteristics of microstrip transmission lines," *IEEE transactions on electronic computers*, no. 2, pp. 185–193, 1967.

[20] S. Kamal, A. S. Mohammed, M. F. Bin Ain, U. Ullah, R. Hussin, Z. Arifin Ahmad, M. Othman, and M. F. Ab Rahman, "A novel negative meander line design of microstrip antenna for 28 ghz mmwave wireless communications," 2020.

[21] A. Ericsson and D. Sjöberg, "Design and analysis of a multilayer meander line circular polarization selective structure," *IEEE Transactions on Antennas and Propagation*, vol. 65, no. 8, pp. 4089–4101, 2017.

[22] D. Ahn, J.-S. Park, C.-S. Kim, J. Kim, Y. Qian, and T. Itoh, "A design of the low-pass filter using the novel microstrip defected ground structure," *IEEE transactions on microwave theory and techniques*, vol. 49, no. 1, pp. 86–93, 2001.

[23] E. Rajo-Iglesias, L. Inclán-Sánchez, J.-L. Vázquez-Roy, and E. García-Muñoz, "Size reduction of mushroom-type ebg surfaces by using edge-located vias," *IEEE Microwave and Wireless Components Letters*, vol. 17, no. 9, pp. 670–672, 2007.

[24] J. Adler, T. Kronauer, and A. N. Barreto, "Hermespy: An open-source link-level evaluator for 6g," *IEEE Access*, vol. 10, pp. 120256–120273, 2022.

[25] NI, "Ettus USRP X410 Specifications," 2023-03-15.